Experimental and Computational Studies on Ruthenium(II) Bis-diimine Complexes of *N,N'*-Chelate Ligand: The Origin of Changes in Absorption Spectra upon Oxidation and Reduction.

Journal:	*Physical Chemistry Chemical Physics*
Manuscript ID	CP-ART-08-2018-005016.R2
Article Type:	Paper
Date Submitted by the Author:	19-Mar-2019
Complete List of Authors:	Tan, Siew San; Universiti Kebangsaan Malaysia Fakulti Sains dan Teknologi, School of Chemical Science and Food Technology, ; Osaka University, Department of Precision Science and Technology, Graduate School of Engineering, 2-1 Yamada-oka; Xiamen University, Jalan Sunsuria, Bandar Sunsuria, Yanagisawa, Susumu; University of the Ryukyus, Department of Physics and Earth Sciences, Faculty of Science, Inagaki, Kouji; Osaka University, Department of Precision Science and Technology, Graduate School of Engineering, 2-1 Yamada-oka Kassim, Mohammad B.; Universiti Kebangsaan Malaysia, School of Chemical Sciences & Food Technology, Faculty of Science and Technology, ; Universiti Kebangsaan Malaysia, Fuel Cell Institute; Osaka University, Department of Precision Science and Technology, Graduate School of Engineering, 2-1 Yamada-oka Morikawa, Yoshitada; Osaka University, Department of Precision Science and Technology, Graduate School of Engineering, 2-1 Yamada-oka

PCCP

PAPER

Experimental and Computational Studies on Ruthenium(II) Bis-diimine Complexes of *N,N'*-Chelate Ligands: The Origin of Changes in Absorption Spectra upon Oxidation and Reduction

Received 00th January 20xx,
Accepted 00th January 20xx

DOI: 10.1039/x0xx00000x

www.rsc.org/

Siew San Tan,*[a,b,c] Susumu Yanagisawa,[e] Kouji Inagaki,[a] Mohammad B. Kassim [a,b,d] and Yoshitada Morikawa [a]

This work presents an interpretation of the origin of changes in absorption spectra upon one-electron oxidation and reduction of two ruthenium polypyridyl complexes based on a combination of UV-Vis spectroelectrochemical experiments and theoretical calculations using the *Gaussian 09* program. A bis-chelating ligand containing a *p*-bromobenzoylthiourea unit connected to 1,10-phenanthroline (phen-*p*-BrBT) has been prepared. Complexation of phen-*p*-BrBT to ruthenium bis-diimine centres, Ru(*N*-*N*)$_2$ [*N*-*N* = 2,2'-bipyridine (bpy) or 1,10-phenanthroline (phen)], affords octahedral Ru(II) tris-diimine complexes that are synthesised and structurally characterised. The two complexes exhibit similar MLCT bands and electronic energy levels owing to the similar electronic structures of the bpy and phen ligands. However, [Ru(phen)$_2$(phen-*p*-BrBT)]$^{2+}$ exhibits a slightly broader visible region $d^6_{Ru} \rightarrow \pi^*_{ligand}$ MLCT (metal-to-ligand-charge transfer) band than [Ru(bpy)$_2$(phen-*p*-BrBT)]$^{2+}$ as expected from a slightly more delocalised π-electron system in the phen diimine ligands. In addition, the $\pi \rightarrow \pi^*$ absorption in the UV is blue-shifted for [Ru(phen)$_2$(phen-*p*-BrBT)]$^{2+}$ relative to that for [Ru(bpy)$_2$(phen-*p*-BrBT)]$^{2+}$, because of greater stabilisation of the bpy HOMO relative to that of phen. The extra C–C bond in phen produces greater delocalisation of electron density leading to a blue-shift in the $\pi \rightarrow \pi^*$ transition. The MLCT band is blue-shifted and diminished in intensity upon oxidation due to stabilisation of the Ru *d*-orbitals by removal of one electron. A new broad absorption band appears in the UV region upon reduction. The new transition is attributed to a blue-shift of the first MLCT transition for [Ru(bpy)$_2$(phen-*p*-BrBT)]$^{2+}$ and a red-shift of the second MLCT transition for [Ru(phen)$_2$(phen-*p*-BrBT)]$^{2+}$. The new transitions originate from destabilisation or stabilisation of the ligand LUMO orbitals relative to the Ru *d*-orbitals. A red-shift of the UV band in the initial complex also contributes to the new band produced upon reduction of [Ru(bpy)$_2$(phen-*p*-BrBT)]$^{2+}$. The new band does not involve an n(C=S) $\rightarrow \pi^*$ transition. Although both complexes show subtle differences in behaviour, their spectral changes are distinct, and the origin of changes in their absorption spectra upon oxidation and reduction is successfully interpreted.

1.0 Introduction

Ruthenium-polypyridine complexes have been widely studied over the past several decades for various applications due to their unique electrochemical and photophysical properties associated with a strong metal-to-ligand-charge transfer (MLCT) absorption[1]. Ruthenium complexes possess six-coordinate octahedral geometry, where the *d*-orbitals split into triply degenerate t_{2g} orbitals at lower energy and doubly degenerate e_g orbitals at higher energy. Ru(II) possesses doubly occupied t_{2g} orbitals and empty e_g orbitals in its low-spin $4d^6$ configuration. The highest occupied molecular orbital (HOMO) of Ru-diimine complexes generally has Ru (d-t_{2g}) character, whereas the lowest unoccupied molecular orbital (LUMO) is typically a π^* orbital localised on the ligands. This configuration results in a MLCT [$d_{Ru} \rightarrow \pi^*_{ligand}$] transition[2,3,4] upon visible light irradiation. Interpretation of the MLCT absorption in ruthenium(II)-polypyridyl complexes generally is straightforward. However, intensity quenching of the MCLT band upon oxidation and a red-shift upon reduction are interesting subjects of discussion.

Ruthenium complexes with chelating *N*-heterocyclic ligands such as 2,2'-bipyridine (bpy) and 1,10-phenanthroline (phen) are often chosen as benchmarks in physicochemical studies of coordination compounds[5,6,7,8]. Placement of substituted bpy or

[a] Department of Precision Science and Technology, Graduate School of Engineering, Osaka University, 2-1 Yamada-oka Suita, Osaka, 565-0871 Japan. Email: siewsan.tan@xmu.edu.my
[b] School of Chemical Science and Food Technology, Faculty of Science and Technology, Universiti Kebangsaan Malaysia, 43600 Bangi, Selangor, Malaysia.
[c] Xiamen University Malaysia, Jalan Sunsuria, Bandar Sunsuria, 43900 Sepang, Selangor, Malaysia.
[d] Fuel Cell Institute, Universiti Kebangsaan Malaysia, 43600 Bangi, Selangor, Malaysia.
[e] Department of Physics and Earth Sciences, Faculty of Science, University of the Ryukyus, 1 Senbaru, Nishihara, Okinawa, 903-0213 Japan.

phen ligands on the ruthenium centre alters the redox chemistry and the luminescence and decay kinetics of MLCT excited states. Spectroelectrochemistry (SEC), which combines electrochemistry with ultraviolet (UV) and visible (Vis) spectroscopy, is a useful tool for analysing electron-transfer processes including the redox chemistry of Ru^{2+} complexes with *N*-heterocyclic ligands[9]. SEC is a multi-response technique capable of interpreting complex reaction mechanisms. Addition or removal of an electron alters the electrochemical and UV-Vis properties of a molecule, a characteristic that has sparked great interest among experimentalists. For example, SEC can determine how the electronic properties of a complex change with protonation, as exemplified by a decrease in the MLCT band and appearance of new band at lower energy in a substituted Ru-bpy complex[10]. Theoretical and computational studies of the electronic structure of Ru-polypyridyl complexes will help to achieve a better understanding of their experimentally observed UV-Vis spectral changes upon oxidation/reduction. The identification and origin of electronic transitions in the optical spectra of the complexes are based on the electronic structures of the isolated bpy or phen ligands. Quantum mechanical methods have recently become an effective computational tool and are widely used to provide useful information regarding frontier orbital energies and band assignments in metal complexes. For example, density functional theory (DFT) and time-dependent DFT (TD-DFT) can establish the absorbance behaviour of protonated and deprotonated complexes[11]. These approaches have been used to determine the relationship between the electrostatic potential distribution and absorption intensities under acidic and basic conditions.

At present, we are interested in carrying out experimental and theoretical studies on the effects of addition or removal of an electron on the electronic properties and origin of the absorption spectra. DFT and TD-DFT are methods of choice to deal with the analyses of frontier molecular orbitals (MOs) and electronic distributions in the complexes and ligands. To the best of our knowledge, this is the first report seeking to determine the origin of changes in the absorption spectra of ruthenium-polypyridyl complexes upon SEC oxidation/reduction using DFT and TD-DFT to investigate the frontier MOs and electronic structures of the ligands. In this paper, we describe the structural, spectroscopic, electrochemical, and UV-Vis spectroelectrochemical properties of two new ruthenium(II) complexes containing *N*,*N*'-chelating diimine ligands (bpy or phen) and the bidentate *p*-bromobenzoyl-*N*'-(1,10-phenanthrolin-5-yl)thiourea (phen-*p*-BrBT) ligand. In addition, we conduct theoretical calculations using Gaussian 09 to characterise the orbitals of the complexes involved in the electronic transition and to gain a deeper understanding of the experimentally observed spectral features.

2.0 Experimental

2.1 Materials and Chemicals

$RuCl_3 \cdot 3H_2O$, lithium chloride, 1,10-phenantroline-5-amine and *p*-bromobenzoyl chloride and 2,2'-bipyridine (bpy) were purchased and used without further purification. The solvents were of analytical reagent grade.

2.2 Spectroscopic and Electrochemical Measurements

Infrared spectra were recorded with an ATR Diamond accessory on an Agilent Cary 630 spectrometer. UV-visible spectra were obtained in a 1-cm quartz cell on a Perkin-Elmer Lambda 35 spectrophotometer. Elemental analyses for C, H, N, and S were performed with a Leco 932 analyser. Mass spectra of $[Ru(bpy)_2(phen\text{-}p\text{-}BrBT)](PF_6)_2$ were recorded on a DIMS 2010 Shimadzu instrument with the ionization energy maintained. ^1H and ^{13}C NMR spectra in DMSO-d_6 solution were recorded on a Bruker Ascend 400 spectrometer. Chemical shifts are reported as parts per million (ppm) relative to Me_4Si. Electrochemical measurements were conducted with a Voltlab PGZ402, Ametek VersaSTAT 4 system. Cyclic voltammograms were measured in a standard three-electrode cell containing a glassy carbon working electrode (4-mm diameter), Ag/AgCl reference electrode (0.01 M $AgNO_3$ and 0.1 M $TBAPF_6$ in CH_3CN,) and a platinum rod auxiliary electrode (2-mm diameter). The ruthenium complexes were investigated as 1 x 10^{-3} M solutions in CH_3CN with 0.1 M tetra-*n*-butylammonium hexafluorophosphate ($TBAPF_6$) supporting electrolyte at a scan rate of 400 mV s^{-1}. Oxygen was displaced from solvents by purging with high-purity nitrogen throughout the analysis. Half-wave potentials were calculated as $E_{1/2} = (E_{pc} + E_{pa})/2$, where E_{pc} and E_{pa} are the cathodic and anodic peak potentials, respectively, and are reported relative to the ferrocene/ferricenium (Fc/Fc^+) redox couple. UV-visible spectroelectrochemical experiments were performed in a thin-layer cell (1.0-mm optical path length), in which a platinum mesh working electrode was placed in HPLC-grade acetonitrile (CH_3CN) containing the samples (1 x 10^{-4} M) and 0.1 M $TBAPF_6$ supporting electrolyte at −20 °C. A platinum wire and a Ag/AgCl electrode in 3 M KCl were used as the counter and reference electrodes, respectively. The potential was fixed about 200 mV beyond the potential of the ruthenium oxidation or reduction wave. The measurements were carried out from 230 to 600 nm with an integration time of 30 s.

2.3 Quantum Chemical Calculations

Electronic structures were calculated by DFT using the Gaussian 09 suite of quantum chemistry programs[12]. Geometries of the molecules were optimised in the ground, oxidised, and reduced states. All geometry optimisation procedures were done by DFT implementing Becke's three-parameter hybrid functional and the restricted Lee-Yang-Parr gradient-corrected functional (RB3LYP)[13,14]. We chose the LANL2DZ effective core potential basis set for the ruthenium atom and the 6-311G (*d*,*p*) split-valence basis set with polarisation for the remaining atoms. Acetonitrile (CH_3CN, ε = 35.7) was chosen as a reference solvent to establish consistency with the experimental results. All vibrational frequency calculations exhibited positive eigenmodes in the optimised geometries. TD-DFT[15,16] calculations were used to interpret the optical spectra by inclusion of a solvent effect with a polarisable continuum model (PCM)[17]. A total of 200 spin-allowed excitation energies were simulated. All computed frontier MOs are displayed with an

isovalue of 0.036 $e^{1/2}$ Bohr$^{-3/2}$. The calculated absorption spectra were generated using Chemissian software[18] with a half-width value of 0.06 eV. The ChemCraft (*v*1.8) visualisation software package was used to represent the calculated structures.

2.4 Synthesis of Ruthenium(II) bis(bipyridine) dichloride, $Ru(bpy)_2Cl_2·H_2O$

The starting complex, $Ru(bpy)_2Cl_2·H_2O$, was prepared according to a published procedure[19]. Its characterisation is reported in our previous paper[20].

2.5 Synthesis of *p*-bromobenzoyl-*N*'(1,10-phenanthrolin-5-yl)-thiourea (phen-*p*-BrBT)

The ligand was synthesised as described in our previous paper[20] by reaction of *p*-bromobenzoyl chloride (1.0 mmol) with ammonium thiocyanate (1.0 mmol) in anhydrous acetone to produce *p*-bromobenzoyl isothiocyanate followed by condensation with 1,10-phenanthroline-5-amine (1.0 mmol) in ethanol. Crystal and molecular structures were determined by single crystal X-ray diffraction as described in this paper. Yield: 68.0%. m.p: 175.2-176.5 °C. IR spectrum (cm^{-1}): ν(N-H) 3596, ν(C-$H_{stretching}$) 3340-3050, ν(C=O) 1676, ν(C=S) 1259, ν(C-N)$_{heterocyclic}$ 1420, ν(C-N)$_{aliphatic}$ 1171. UV-Vis spectrum in CH_2Cl_2 [λ_{max} (nm), ε (L mol^{-1} cm^{-1})]: 270 (56,517), 231 (59,724). Mass spectrum (*m/z*): 458.99 (459.0 theory), [Phen-*p*-BrBT-Na]$^+$; 437.10 (437.00 theory), [Phen-*p*-BrBT-H]$^+$; 260.02 (260.05 theo*ry*), [Phen-NH-C=S-Na]$^+$; 238.04 (238.05 theory), [Phen-NH-C=S]$^+$. Anal., Calc: C, 54.93; H, 3.00; N, 12.81; S, 7.33. Found: C, 56.55; H, 4.05; N, 12.14; S, 7.37. ^{1}H NMR (400 MHz, DMSO-*d*^{6}), δ: 12.53 (s, 1H), 11.97 (s, 1H), 9.13 (t, 2H), 8.16 (s, 1H), 7.99 (m, 2H), 8.53 (d, 1H), 8.48 (d, 1H), 7.85-7.77 (m, 4H). Luminescence, [λ_{em}(nm) in CH_2Cl_2]: 375, φ_s= 2.29 x 10^{-2}.

2.5.1 Single Crystal X-ray of Phen-p-BrBT Ligand

A yellow crystal of phen-*p*-BrBT was grown by slow diffusion of acetone into an ethanolic solution of the compound. Single crystal X-ray diffraction measurements were carried out on a Bruker SMART APEX CCD area-detector diffractometer equipped with a graphite monochromator for data collection at 296(2) K. Unit cell dimensions and data collection were performed with MoK_α radiation (λ= 0.71073 Å). The structure was solved by direct methods using SHELX and refined by full-matrix least-squares on F^2 (Sheldrick, 2013). The experimental details of the molecular structure and structural refinement data of the ligand are summarised in Table 1. The bond lengths and bond angles of the ligand (Table 2) are within normal ranges[21].

In the phen-*p*-BrBT crystal, the bromobenzoyl and 1,10-phenanthroline moieties adopt *cisoid* and *transoid* conformations, across the C8–C2 and C8–N1 bonds, respectively. The conformation of the molecule is non-planar with respect to the bromobenzoyl and 1,10-phenanthroline moieties with dihedral O1A–C7–N1–C8, S1–C8–N1–C7, and N2–C8–N1–C7 angles of –17.04, –174.13, and 3.73°, respectively. The bromine atom attached to the *para* position is aligned in an *antiperiplanar* conformation with a –177.77° C2–C3–C4–-Br1 torsion angle. There is an intramolecular N2–H2A···O1A hydrogen bond in the phen-*p*-BrBT structure, which results in the formation of a pseudo six-membered (N2–C8–N1–C7–O1A···H2A) ring (Fig. 1). The length of the C–N bonds (N1–C7, N1–C8, N2–C8, and N2–C13) in the thiourea fragment range from 1.429(4) to 1.331(4) Å, which are intermediate to values expected for single and double C–N bonds (1.47 and 1.27 Å, respectively). The observations suggest that there is a π-electron delocalisation over the pseudo six membered-ring. Among these C–N bonds, N2–C13 is the longest, which is indicative of a C(sp^2)–N(sp^2) single bond. N2–C8, which is the shortest, exhibits more double bond character. The existence of the intramolecular hydrogen bond makes the N2–C8–N1 bond angle (115.2°) smaller than the normal value (120°). The thiourea group is *cis-trans* with respect to phenanthroline and bromobenzoyl moieties across the C8–N1 bonds. In light of this feature, electronic delocalisation from the bromobenzoyl group may decrease the bond order of the C=O group, but no changes in geometry of the phenanthroline unit are expected. The likelihood of electronic delocalisation is consistent with the slightly shorter C=O bond length [1.216(3) Å] as compared with the reported C=O distance in an unsubstituted phenyl ring [1.222(2) Å] [22]. The small decrease in bond length may be due to the weaker electron withdrawing effect of bromine atom at the *para* position. The packing of phen-*p*-BrBT exhibits a weak C5–H5···N4 intermolecular contact between molecules as shown in Table 3.

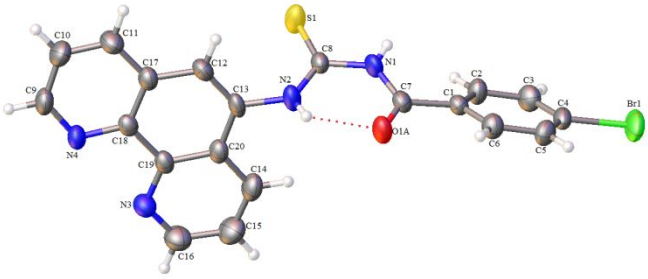

Fig. 1 The molecular structure of phen-*p*-BrBT drawn with 50% probability ellipsoids. The dashed line indicates the intramolecular hydrogen bond resulting in a pseudo six-membered ring.

Table 1 Crystal data, data collection and structure refinement of phen-*p*-BrBT

Data	Phen-*p*-BrBT
Empirical formula	$C_{20}H_{13}N_4O_1S_1Br_1$
Formula weight (g/mol)	437.30
Crystal system	Triclinic
Space group	*P*(1)
a (Å)	8.8883(9)
b (Å)	9.4264(9)
c (Å)	12.0358(12)
α (°)	71.714(6)
β (°)	80.483(7)
γ (°)	80.791(7)
V (Å^3)	937.99(17)
Z	2
F(0 0 0)	440

p(mg/m^3)	1.548
Absorption coefficient, μ (mm^{-1})	2.320
Crystal size (mm)	0.03 x 0.22 x 0.28
Theta Min-Max (˚)	3.1-25.1
Dataset	-10: 10; -11: 11; -14: 14
Tot., Uniq. Data, R(int)	13628, 3351, 0.062
Observed Data [I > 2.0 sigma(I)]	2224
N_{ref}, N_{par}	3321, 269
R, *wR2*, S	0.0380, 0.0822, 1.00

Table 2 Selected bond lengths and angle for phen-*p*-BrBT

Bond lengths (Å)	**Phen-*p*-BrBT**
N1-C7	1.372(4)
N1-C8	1.391(4)
N2-C8	1.331(4)
N2-C13	1.430(4)
O1A-C7	1.216(3)
S1-C8	1.654(3)
C4-Br1	1.900(3)
C1-C7	1.491(4)
Bond angle(°)	
N1-C7-C1	115.2(3)
N1-C8-S1	119.9(2)
N2-C8-N1	115.2(3)
N2-C8-S1	124.9(2)
O1A-C7-N1	122.4(3)
O1A-C7-C1	122.3(3)
C7-N1-C8	129.0(3)
C8-N2-C13	124.6(3)

Table 3 Hydrogen bond parameter for phen-*p*-BrBT (Å and deg.)

D-H···A	Type	D-H	H···A	D···A	D-H···A
N2-H2A···O1A	Intra	0.80	2.04	2.668(3)	135
C5-H5···N4^{i}	Inter	0.93	2.54	3.289(5)	137

Symmetry code: (i)= 1+x,y,-1+z

2.6 Synthesis of the ruthenium(II) bipyridyl *p*-bromobenzoyl-*N*'-(1,10-phenanthrolin-5-yl)-thiourea [Ru(bpy)$_2$(phen-*p*-BrBT)](PF$_6$)$_2$

The principal complexes were prepared using our previously published method[11]. The method is a mild synthetic approach with simple purification protocols and shorter reaction time. The synthetic details are provided in the Supplementary Information. The product was obtained as an orange precipitate (yield = 71.5%). Molecular formula; $C_{40}H_{29}N_8OSBrP_2F_{12}Ru$. CHNS analysis, Calc: C(42.12), H(2.56), N(9.82), S(2.81); Found: C(41.96), H (3.09), N(10.63), S(2.77). IR spectrum (cm^{-1}): ν(N-H) 3392, ν(C-N$_{heterocyclic}$) 1446, ν(C-N$_{aliphatic}$) 1165, ν(C-C)$_{stretching}$ 1584-1465, ν(C=O) 1670, ν(C=S) 1244, ν(uncoordinated PF_6^-) 830. UV/Vis data; λ_{max}, nm/CH_3CN, ε (L mol^{-1} cm^{-1}): 286 (67,245), 455 (14,667). Mass spectrum (m/z)$^+$: 995.06 (995.01 theory), [Ru(bpy)$_2$(phen-*p*-BrBT)(PF$_6$)]$^+$; 425.03 (426.02 theory), [Ru(bpy)$_2$(phen-*p*-BrBT)(PF$_6$)]$^{2+}$/2. ^{1}H NMR (400 MHz, DMSO-d^6), δ: 12.78 (s, 1H), 12.14 (s, 1H), 8.91-8.81 (m, 4H), 8.75 (dd, 1H), 8.68 (s, 1H), 8.16-8.11 (m, 4H), 8.23 (t, 2H), 8.19 (dd, 1H), 8.01 (m, 2H), 7.96-7.88 (m, 2H), 7.88-7.80 (m, 4H), 7.60 (m, 2H), 7.67 (d, 1H), 745-7.37 (m, 2H), 7.56 (d, 1H). ^{13}C NMR (400 MHz, DMSO-d^6), δ: 182.14 (C=S), 171.21 (C=O).

2.7 Synthesis of ruthenium(II) bis(phenanthroline) *p*-bromobenzoyl-*N*'-(1,10-phenanthrolin-5-yl)-thiourea bis(hexafluorophosphate) [Ru(phen)$_2$(phen-*p*-BrBT)](PF$_6$)$_2$

The molecule was prepared according to the previously described procedure except that [Ru(phen)$_2$Cl$_2$·H$_2$O (0.064 mmol) was used instead of the bpy analogue. The product was obtained as a deep red precipitate (yield = 63.5%). Molecular formula: $C_{44}H_{29}N_8OSBrP_2F_{12}Ru$. CHNS analysis, Calc: C(44.46), H(2.46), N(9.43), S(2.70); Found: C(43.79), H (2.61), N(9.19), S(2.06). IR spectrum (cm^{-1}): ν(NH) 3631, ν(C-N$_{heterocyclic}$) 1458, ν(C-N$_{aliphatic}$) 1168, ν(C-C)$_{stretching}$ 1583-1481, ν(C=O) 1670, ν(C=S) 1261, ν(uncoordinated PF_6^-) 831. UV/Vis data; λ_{max}, nm/CH_3CN, ε (L mol^{-1} cm^{-1}): 266 (80,246), 455 (13,308). ^{1}H NMR (400 MHz, DMSO-d^6), δ: 12.53 (s, 1H), 11.97 (s, 1H), 8.39-8.37 (m, 4H), 8.55 (dd, 1H), 8.17 (s, 1H), 8.40-8.36 (m, 4H), 9.15-9.12 (m, 2H), 8.48 (dd, 1H), 8.77-8.75 (m, 2H), 8.08-8.06 (m, 2H), 8.02-7.99 (m, 2H), 7.85-7.80 (m, 4H), 7.77-7.75 (2H), 7.23-7.73 (2H). ^{13}C NMR (400 MHz, DMSO-d^6), δ: 182.35 (C=S), 167.89 (C=O). The synthetic reaction scheme is illustrated in Fig. 2.

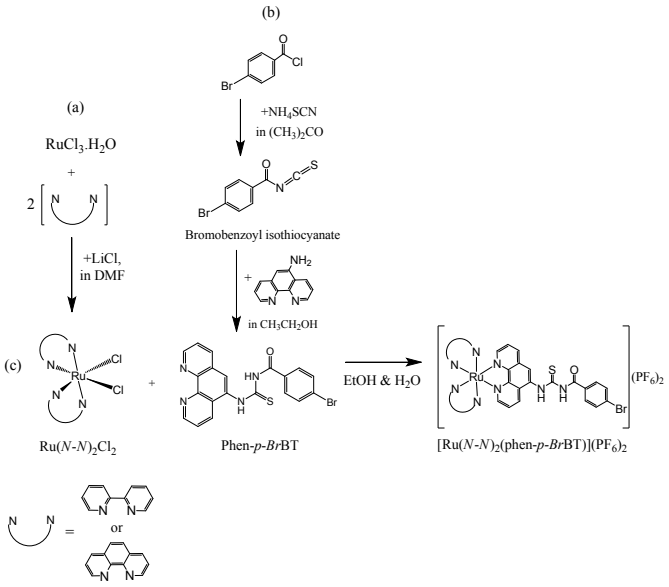

Fig. 2 Reactions scheme for the synthesis of [Ru(*N*-*N*)$_2$(phen-*p*-BrBT)](PF$_6$)$_2$ and [Ru(*N*-*N*)$_2$(phen-*p*-BrBT)](PF$_6$)$_2$.

3.0 Result and Discussion

[Ru(bpy)$_2$(phen-*p*-BrBT)](PF$_6$)$_2$ and [Ru(phen)$_2$(phen-*p*-BrBT)](PF$_6$)$_2$ were obtained by in situ reaction of Ru(*N*-*N*)$_2$Cl$_2$·H$_2$O [*N*-*N* = 2,2'-bipyridine (bpy) or 1,10-phenanthroline (phen,)] with phen-*p*-BrBT. The cationic fragments of the isolated complexes have an overall charge of 2+. The oxidised and reduced fragments have charges of 3+ and 1+, respectively. The complexes have been characterized by

elemental analyses and by IR, UV-Vis, ^{1}H and ^{13}C NMR spectroscopy as described above.

3.1 The Effect of Changes in N-N Diimine Ligand on Optical Absorption Spectra of Ru(II) Complexes

The optical absorption spectra of the ruthenium polypyridyl complexes are typical of those with bpy and phen ligands. Fig. 3a displays the spectra of $[Ru(bpy)_2(phen\text{-}p\text{-}BrBT)]^{2+}$ and $[Ru(phen)_2(phen\text{-}p\text{-}BrBT)]^{2+}$ in CH_3CN. The complexes exhibit strong absorption bands in the UV-Vis region at 286 nm (67,200 mol^{-1} dm^3 cm^{-1}) and 266 nm (80,200 $mol^{-1}dm^3cm^{-1}$) for $[Ru(bpy)_2(phen\text{-}p\text{-}BrBT)](PF_6)_2$ and $[Ru(phen)_2(phen\text{-}p\text{-}BrBT)](PF_6)_2$, respectively. The bands are unambiguously assigned to spin-allowed $\pi \rightarrow \pi^*$ ligand-centred (LC) transitions. This transition involves the excitation of electrons from the filled π to vacant π^* orbitals of the ligands[15,20]. Both complexes exhibit a broad band of lower intensity in the visible region at 455 nm, which is assigned to a spin-allowed MLCT transition similar to other Ru(II) polypyridyl complexes [1,2].

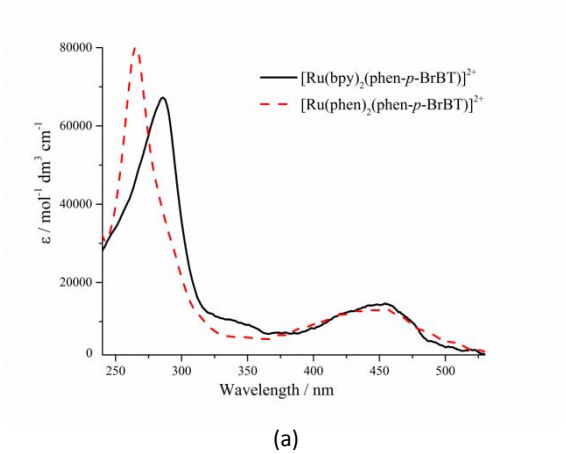

(a)

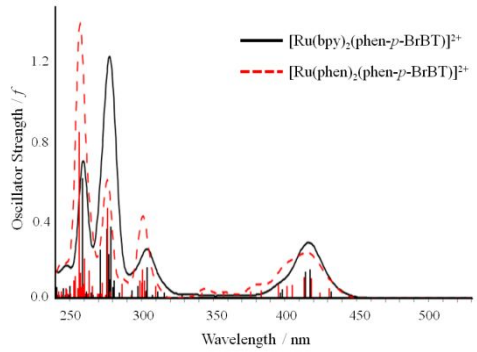

(b)

Fig. 3 Experimental (a) and calculated (b) optical absorption spectra of Ru(II) complexes.

The shape of the $[Ru(bpy)_2(phen\text{-}p\text{-}BrBT)](PF_6)_2$ absorption band in the UV differs little from that of $[Ru(phen)_2(phen\text{-}p\text{-}BrBT)](PF_6)_2$. However, the $[Ru(phen)_2(phen\text{-}p\text{-}BrBT)]^{2+}$ band is shifted hypsochromically by 20 nm relative to that of $[Ru(bpy)_2(phen\text{-}p\text{-}BrBT)]^{2+}$, which demonstrates the impact of the phen for bpy replacement. The extended π-electron system of phenanthroline leads to a greater energy gap for the $\pi_L \rightarrow \pi^*_L$ transition (Table 4). In the visible region, a slightly broader MLCT absorption band is observed for $[Ru(phen)_2(phen\text{-}p\text{-}BrBT)]^{2+}$, which is probably due to greater π-system delocalisation in the phen complex. TD-DFT calculations confirm these points.

3.2 Electronic Structures and Theoretical Absorption Spectra

DFT calculations using the LANL2DZ/6311G mixed basis set in acetonitrile were performed to gain further insight into the electronic structure of the complexes. The orbital energies and isosurfaces of frontier molecular orbitals for the isolated bpy and phen ligands are presented in Table 4. Similar electron cloud distributions in the frontier MOs are arranged in the same row of the table. Table 5 shows contour plots of the frontier molecular orbitals (HOMO-3 to LUMO+3) and the principal ligand character for both complexes. The composition and nature of the relevant transitions for both complexes are shown in Table I and II in the Supplementary Data. The three highest occupied molecular orbitals (HOMOs) in both complexes are nearly degenerate and are mainly ruthenium 4*d* (t_{2g}) in character. The HOMO-3 orbital of both complexes is dominated by the C=S orbital with small contributions from the ruthenium centre in $[Ru(phen)_2(phen\text{-}p\text{-}BrBT)]^{2+}$ and no Ru contribution in $[Ru(bpy)_2(phen\text{-}p\text{-}BrBT)](PF_6)_2$. The lowest unoccupied molecular orbitals (LUMOs) of the compounds have no π^* character delocalised over the ligands. The main contributor to the LUMO of $[Ru(bpy)_2(phen\text{-}p\text{-}BrBT)](PF_6)_2$ is the LUMO of the bpy and phen on BT moiety, whereas LUMO+1 (phen) is the main component of the $[Ru(phen)_2(phen\text{-}p\text{-}BrBT)](PF_6)_2$ LUMO. We note that the shapes of the LUMO (bpy) and LUMO+1 (phen) orbitals are essentially the same. Consequently, the spin-allowed MLCT bands of the corresponding complexes are quite similar, and their electronic energy levels are almost the same.

Table 4 Frontier molecular orbitals (HOMO-1 to LUMO+2) of isolated phen and bpy. MOs with equivalent electron cloud distributions are displayed in the same row for comparison.

FMO	Bipyridine (bpy)	FMO	Phenanthroline (phen)
LUMO+2	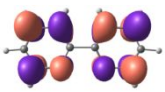 (44) -0.663 eV	LUMO+3	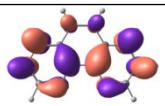 (51) 0.146 eV
LUMO+1	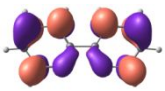 (43) -1.080 eV	LUMO+2	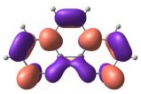 (50) -0.590 eV
LUMO	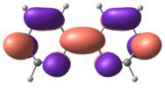 (42) -1.762 eV	LUMO+1	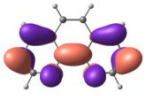 (49) -1.774 eV

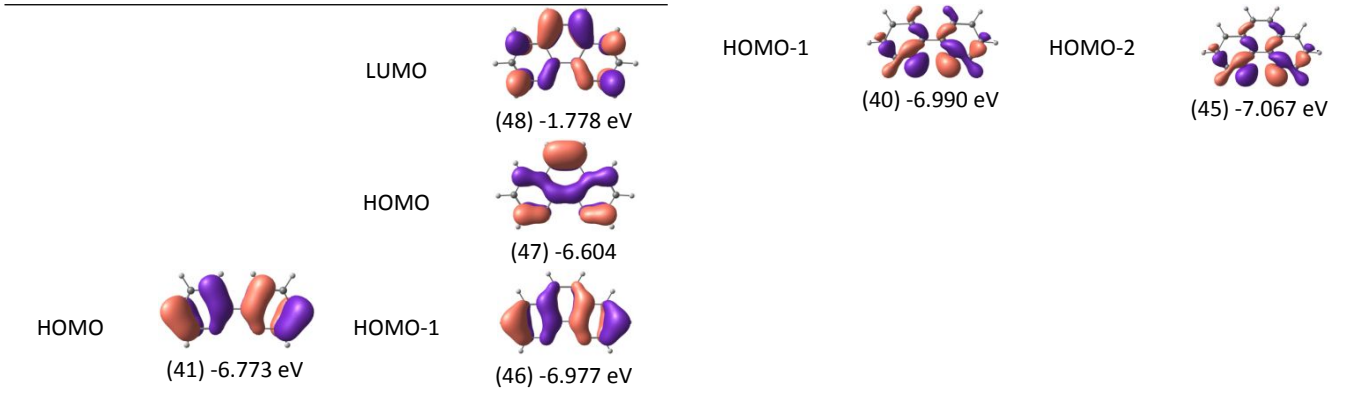

Table 5 Isocontour plots and energies of selected molecular orbitals (HOMO-3 to LUMO+3) and their principal ligand character for $[Ru(bpy)_2(phen\text{-}p\text{-}BrBT)]^{2+}$ and $[Ru(phen)_2(phen\text{-}p\text{-}BrBT)]^{2+}$ in acetonitrile with an isovalue of 0.036 $e^{1/2}$ $Bohr^{-3/2}$.

Orbitals	Frontier MO with energies $[Ru(bpy)_2(phen\text{-}p\text{-}BrBT)]^{2+}$	Principal ligand character	Frontier MO with energies $[Ru(phen)_2(phen\text{-}p\text{-}BrBT)]^{2+}$	Principal ligand character
LUMO+3	-2.663 eV	LUMO (phen-*p*-BrBT) LUMO (bpy)	-2.651 eV	LUMO+1 (phen) on the other two phen moieties
LUMO+2	-2.701 eV	LUMO (phen-*p*-BrBT) LUMO (bpy)	-2.681 eV	LUMO+1 (phen) on BT moiety
LUMO+1	-2.722 eV	LUMO (phen-*p*-BrBT) LUMO (bpy)	-2.746 eV	LUMO (phen) on BT moiety
LUMO	-2.810 eV	LUMO+1 (phen-*p*-BrBT) LUMO (bpy)	-2.819 eV	LUMO+1 (phen) on BT moiety
HOMO	-6.311 eV	Ru-*d*	-6.329 eV	Ru-*d*
HOMO-1	-6.449 eV	Ru-*d*	-6.426 eV	Ru-*d* and C=S
HOMO-2	-6.482 eV	Ru-*d*	-6.433 eV	Ru-*d*

HOMO-3	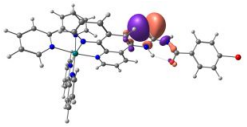 -6.689 eV	C=S	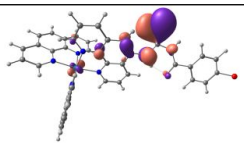 -6.645 eV	C=S and Ru-d

We used TD-DFT calculations to analyse the optical absorption spectra. The lowest 200 spin-allowed excited states in acetonitrile were taken into account for calculations of the optimised complexes. The calculated spectra (Fig. 3b) are in excellent agreement with the observed spectra (Fig. 3a) in terms of peak positions and relative intensities of the MLCT and π ⟶ π* bands. TD-DFT shows the lowest energy MLCT band to lie in the visible region at λ_{max} = 418 and 414 nm for $[Ru(bpy)_2(phen\text{-}p\text{-}BrBT)]^{2+}$ and $[Ru(phen)_2(phen\text{-}p\text{-}BrBT)]^{2+}$. These bands arise from the HOMO-2 ⟶ LUMO+2 and HOMO-2 ⟶ LUMO+3 transitions, respectively. The MLCT bands of the complexes are quite similar owing to the similar shapes and energy levels of their molecular orbitals as shown in Fig. 4. The calculation for $[Ru(phen)_2(phen\text{-}p\text{-}BrBT)](PF_6)_2$ predicts a slightly broader MLCT in the visible region, which agrees with the experimental result. This is due to the greater number of vertical MLCT excitations calculated for $[Ru(phen)_2(phen\text{-}p\text{-}BrBT)]^{2+}$ as indicated by the vertical lines in Fig. 3b.

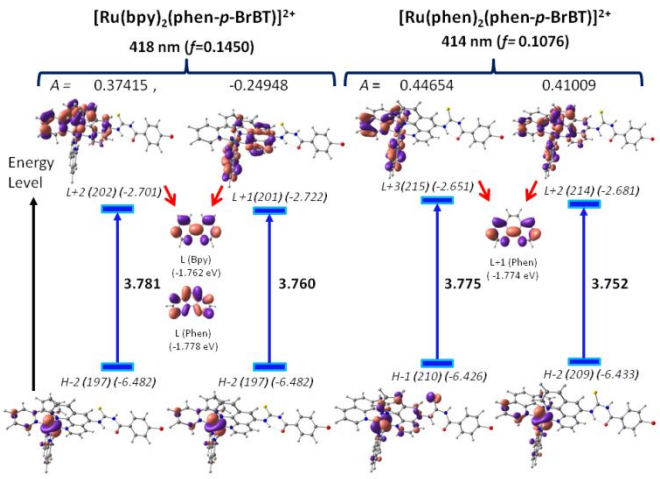

Fig 4. Energy level diagrams of complexes in the visible region and frontier MOs of the ligands that contribute to the MLCT transition.

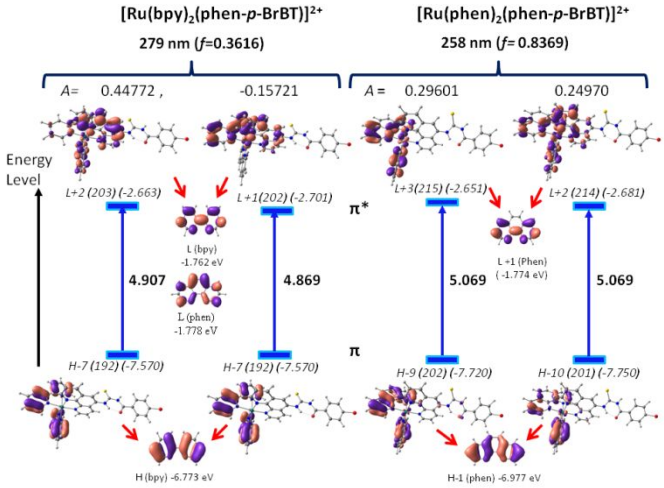

Fig. 5 Energy level diagrams of complexes in the UV region and frontier MOs of the ligands that contribute to the π ⟶ π* transition.

The 279-nm absorption of $[Ru(bpy)_2(phen\text{-}p\text{-}BrBT)]^{2+}$, which has the greatest oscillator strength in the UV region, is attributed to the HOMO-7 ⟶ LUMO+2 and HOMO-7 ⟶ LUMO+1 transitions as shown in Fig. 5. The strongest UV absorption band of $[Ru(phen)_2(phen\text{-}p\text{-}BrBT)]^{2+}$, which is centred at 258 nm, arises mainly from the HOMO-9 ⟶ LUMO+3 and HOMO-10 ⟶ LUMO+2 transitions as shown in Fig. 5. The calculated absorption maximum is shifted hypsochromically by 21 nm for $[Ru(phen)_2(phen\text{-}p\text{-}BrBT)]^{2+}$ relative to $[Ru(bpy)_2(phen\text{-}p\text{-}BrBT)]^{2+}$ primarily due to stabilisation of the HOMO level of its phen moiety. We note that the HOMO-7 of $[Ru(bpy)_2(phen\text{-}p\text{-}BrBT)]^{2+}$ mainly comprises the bpy HOMO, whereas the HOMO-9 and HOMO-10 of $[Ru(phen)_2(phen\text{-}p\text{-}BrBT)]^{2+}$ come from the HOMO-1 of phen. In addition, the LUMO+3 of $[Ru(bpy)_2(phen\text{-}p\text{-}BrBT)]^{2+}$ comprises the LUMOs of the bpy and phen units, whereas the LUMO+3 of $[Ru(phen)_2(phen\text{-}p\text{-}BrBT)]^{2+}$ is primarily LUMO+1 (phen) in character. The blue-shift of the $[Ru(phen)_2(phen\text{-}p\text{-}BrBT)]^{2+}$ transition is therefore attributed to the stabilisation provided by the more extensive π-delocalisation of the phen HOMO-1 relative to the HOMO of bpy. To further confirm this point, we calculated the absorption spectra of the isolated bpy and phen ligands (Fig. 6a). The energy level diagrams representing the π ⟶ π* transitions at 272 and 252 nm for bpy and phen, respectively, are shown in Fig. 6b. The absorption band of bpy is assigned to the HOMO (π) ⟶ LUMO (π*) transition, whereas the absorption band of phen has HOMO-1 (π) ⟶ LUMO+1 (π*) character. One should notice that the electron cloud distributions of the frontier MOs are identical and that the extra C–C bond in the phen ligand results in greater π-electron delocalisation and thus lower electronic energy

of the occupied MO. HOMO-1 is greatly stabilised relative to LUMO+1 resulting in a blue-shift in the absorption band of phen. The electronic structure analysis of the isolated ligands provides solid evidence for the optical properties of bpy and phen and the resulting shifts in their absorption spectra. The TD-DFT calculations also replicate the slightly broader MLCT absorption band and blue-shifted π → π* band of $[Ru(phen)_2(phen\text{-}p\text{-}BrBT)]^{2+}$, which substantiates the accuracy of our calculations.

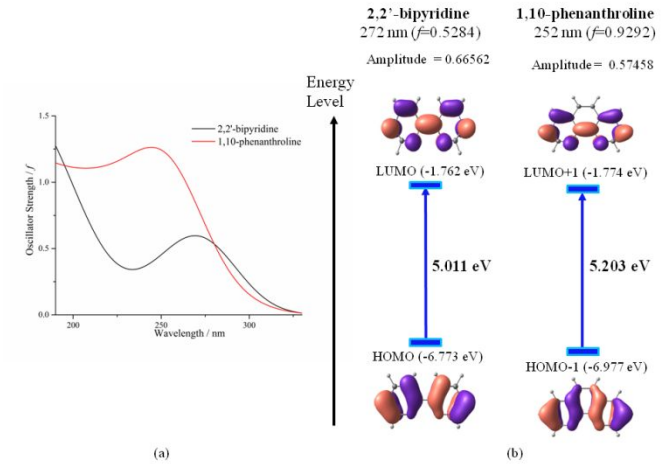

Fig. 6 Comparison between the calculated optical absorption spectra (a) and energy level diagrams (b) associated with the π → π* transitions of 2,2'-bipyridine and 1,10-phenanthroline.

3.3 The Effect of the *N-N* Diimine Ligand on Electrochemical Properties

The electronic effects of both complexes were evaluated in terms of their redox properties, which are listed in Table 6. The ratio of the cathodic to anodic peak currents (i_{pc}/i_{pa}) is generally 1.0, which is consistent with chemically reversible oxidation and reduction of reactions[1]. The complexes exhibit a reversible oxidation at positive potentials. The half-wave potentials, $E_{1/2}^{ox}$, at +0.911 [eq (1)] and +0.893 V [eq (2)] versus Fc/Fc^+ for $[Ru^{II}(bpy)_2(phen\text{-}p\text{-}BrBT)]^{2+}$ and $[Ru^{II}(phen)_2(phen\text{-}p\text{-}BrBT)]^{2+}$, respectively, correspond to the metal-centred Ru(II)/Ru(III) oxidations:

$$[Ru^{II}(bpy)_2(phen\text{-}p\text{-}Br)]^{2+} \longrightarrow [Ru^{III}(bpy)_2(phen\text{-}p\text{-}Br)]^{3+} + 1e \quad E_{1/2} = +0.911\ V \quad (1)$$

$$[Ru^{II}(phen)_2(phen\text{-}p\text{-}Br)]^{2+} \longrightarrow [Ru^{III}(phen)_2(phen\text{-}p\text{-}Br)]^{3+} + 1e \quad E_{1/2} = +0.893\ V \quad (2)$$

Three reversible reduction processes are observed at negative potentials and are tentatively assigned to ligand-centred reactions. The first reduction occurs at −1.318 [eq (3)] and −1.324 V [eq (4)] for $[Ru^{II}(bpy)_2(phen\text{-}p\text{-}BrBT)]^{2+}$ and $[Ru^{II}(phen)_2(phen\text{-}p\text{-}BrBT)]^{2+}$, respectively. The first electron is added to the LUMO of each complex, which is associated with the ligand π* orbitals, affording the species $[Ru^{II}(bpy)_2(phen\text{-}p\text{-}BrBT)]^{1+}$ and $[Ru^{II}(phen)_2(phen\text{-}p\text{-}BrBT)]^{1+}$. This assignment is further established by optical absorption SEC and DFT calculations. The other reversible reductions are located at −1.765 and −1.944 V for $[Ru^{II}(bpy)_2(phen\text{-}p\text{-}BrBT)]^{2+}$ and −1.802 and −1.948 V for $[Ru^{II}(phen)_2(phen\text{-}p\text{-}BrBT)]^{2+}$. The small differences in oxidation and reduction potentials between the two complexes indicate that these values are relatively uninfluenced by the identity of the diimine ligand.

$$[Ru^{II}(bpy)_2(phen\text{-}p\text{-}Br)]^{2+} + e \longrightarrow [Ru^{II}(bpy)_2(phen\text{-}p\text{-}Br)]^{1+} \quad E_{1/2} = -1.318\ V \quad (3)$$

$$[Ru^{II}(phen)_2(phen\text{-}p\text{-}Br)]^{2+} + e \longrightarrow [Ru^{II}(phen)_2(phen\text{-}p\text{-}Br)]^{1+} \quad E_{1/2} = -1.324\ V \quad (4)$$

Table 6 Electrochemical data for the ruthenium complexes in dry CH_3CN/0.1 M $TBAPF_6$ at 298 K [a]

Complexes	Oxidation $[E_{1/2}\ (V)]$ [b]	Reduction $[E_{1/2}\ (V)]$ [b]		
$[Ru^{II}(bpy)_2(phen\text{-}p\text{-}BrBT)]^{2+}$	+0.911	−1.318	−1.765	−1.944
$[Ru^{II}(phen)_2(phen\text{-}p\text{-}BrBT)]^{2+}$	+0.893	−1.324	−1.802	−1.948

[a] Reference electrode- Ag/AgCl, scan rate = 400 mVs^{-1}

[b] $E_{1/2} = 0.5(E_{pc} - E_{pa})$, where E_{pa} and E_{pc} are anodic and cathodic peak potential, respectively, in V versus Fc/Fc^+.

3.3.1 The Origin of Electrochemical Properties

To explore the electrochemical behaviour of the complexes, theoretical calculations were conducted by DFT/B3LYP. The energies of the HOMO and LUMO can be calculated from eq (5) and (6), respectively.

$$E_{HOMO} = E[Ru^{II}(bpy)_2(phen\text{-}p\text{-}Br)]^{2+} - E[Ru^{III}(bpy)_2(phen\text{-}p\text{-}Br)]^{3+} \quad (5)$$

$$E_{LUMO} = E[Ru^{II}(bpy)_2(phen\text{-}p\text{-}Br)]^{1+} - E[Ru^{II}(bpy)_2(phen\text{-}p\text{-}Br)]^{2+} \quad (6)$$

Table 7 Calculated total energies and HOMO and LUMO energies of the complexes in three different oxidation states

Oxidation State	Total Energy / eV	
	$[Ru(bpy)_2(phen\text{-}p\text{-}BrBT)]^{2+}$	$[Ru(phen)_2(phen\text{-}p\text{-}BrBT)]^{2+}$
$[Ru^{II}(bpy)_2(phen\text{-}p\text{-}Br)]^{2+}$	−139,367.878	−143,517.491
$[Ru^{III}(bpy)_2(phen\text{-}p\text{-}Br)]^{3+}$	−139,361.946	−143,511.548
$[Ru^{II}(bpy)_2(phen\text{-}p\text{-}Br)]^{1+}$	−139,370.932	−143,520.548
$Energy_{HOMO/LUMO}$		
E_{HOMO}	−5.932	−5.943
E_{LUMO}	−3.053	−3.057

The oxidation potential corresponds to electron extraction from the HOMO, while the reduction potential is associated with electron addition to the LUMO. The HOMO and LUMO energies of the complexes differ by only 0.011 and 0.004 eV, respectively. These small energy differences point to the limited influence of ligand

composition on the redox potentials. The calculated results are in good agreement with the experimental data.

3.4 Optical Absorption Spectroelectrochemistry (UV-Vis SEC)

The redox behaviour of the complexes was further investigated by UV-Vis SEC to validate the assignment of the optical bands. We first studied the tris(2,2'-bipyridine)ruthenium(II) hexafluorophosphate complex, $[Ru^{II}(bpy)_3](PF_6)_2$, as a basis for comparison. Fig. 7 displays the spectral changes upon oxidation and reduction of $[Ru(bpy)_3]^{2+}$. As expected from their electrochemical properties, the SEC behaviour of the title complexes is similar to that of $[Ru(bpy)_3]^{2+}$. Fig. 8 and Fig. 9 show the UV-Vis spectral changes upon oxidation and reduction of the title complexes, respectively. Oxidation of both complexes involves removal of an electron from the metal orbital resulting in a $4d^5$ Ru^{III} configuration and a suppression of the MLCT band. The diminished intensity of the 453-455 nm absorption upon $Ru^{II} \rightarrow Ru^{III}$ oxidation supports its assignment as an MLCT band. The oxidations of $[Ru(bpy)_2(phen\text{-}p\text{-}BrBT)]^{2+}$ and $[Ru(phen)_2(phen\text{-}p\text{-}BrBT)]^{2+}$ show three (258, 299, and 328 nm) and two (246 and 360 nm) isosbestic points, respectively (Fig. 8). Oxidation of $[Ru(bpy)_2(phen\text{-}p\text{-}BrBT)]^{2+}$ produces a collapse of the $\pi \rightarrow \pi^*$ band at 285 nm accompanied by a noticeable red-shift, which is indicative of a ruthenium-based oxidation[23]. The bands are regenerated when a potential of 0.0 V is applied, which indicates that the oxidation is fully reversible.

UV-Vis SEC of $[Ru(bpy)_2(phen\text{-}p\text{-}BrBT)]^{2+}$ and $[Ru(phen)_2(phen\text{-}p\text{-}BrBT)]^{2+}$ shows parallel spectral changes upon application of a reducing potential of −1500 mV vs. Ag/AgCl (Fig. 9). No well-defined isosbestic points are observed during reduction. One-electron reduction of the title complexes to +1 species produces no significant changes in the MLCT bands. However, the spectra of the reduced complexes are slightly red-shifted. Similar to the behaviour of $[Ru(bpy)_3]^{2+}$ (Fig. 7b), broad absorptions appear at 369 and 340 nm upon reduction of $[Ru(bpy)_2(phen\text{-}p\text{-}BrBT]^{2+}$ and $[Ru(phen)_2(phen\text{-}p\text{-}BrBT)]^{2+}$, respectively. This is primarily a manifestation of the MLCT, and not a reduction in energy of the $n(C{=}S) \rightarrow \pi^*$ (BT) transition[24]. Further explanation will be provided by subsequent DFT calculations. The changes with time upon UV-Vis spectroelectrochemical oxidation and reduction are listed in Tables 8 and 9, respectively.

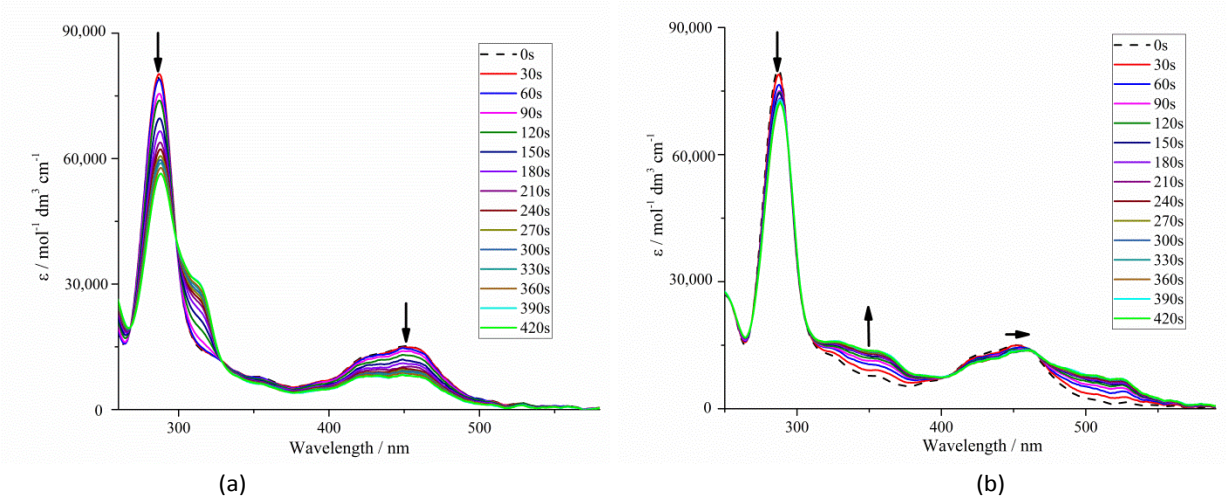

Fig. 7 UV-Vis Spectroelectrochemical experiments showing changes with time upon (a) oxidation at 1200 mV and (b) reduction at -1500 mV of $[Ru(bpy)_3]^{2+}$. The initial spectra are shown as dashed black lines. Arrows indicate the changes upon oxidation or reduction.

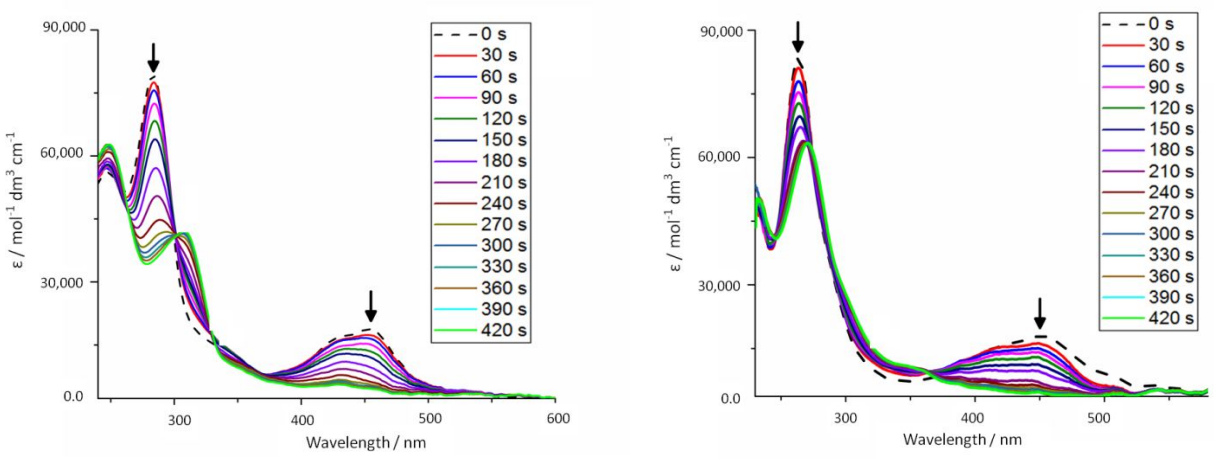

Fig. 8 UV-Vis spectroelectrochemical experiments showing changes with time on oxidation of (a) $[Ru(bpy)_2(phen\text{-}p\text{-}BrBT)]^{2+}$ and (b) $[Ru(phen)_2(phen\text{-}p\text{-}BrBT)]^{2+}$ at 1200 mV vs. Ag/AgCl. The initial spectrum is shown as a dashed black line. Arrows indicate the changes upon one-electron oxidation.

Table 8. UV-Vis spectroelectrochemical data as a function of time upon oxidation of (a) $[Ru(bpy)_2(phen\text{-}p\text{-}BrBT)]^{2+}$ and (b) $[Ru(phen)_2(phen\text{-}p\text{-}BrBT)]^{2+}$ at 1200 mV vs. Ag/AgCl.

Time / s	$[Ru(bpy)_2(phen\text{-}p\text{-}BrBT)]^{2+}$		$[Ru(phen)_2(phen\text{-}p\text{-}BrBT)]^{2+}$	
	Absorption λ_{max} / nm (ε / $Lmol^{-1}cm^{-1}$)		Absorption λ_{max} / nm (ε / $Lmol^{-1}cm^{-1}$)	
0	282.3 (79,215)	452.2 (17,503)	263.7 (83,617)	448.6 (15,401)
30	283.5 (77,498)	452.2 (16,415)	263.7 (80,712)	448.6 (15,166)
60	283.5 (76,607)	452.2 (15,215)	263.7 (78,294)	448.6 (15,011)
90	284.1 (72,608)	452.2 (14,088)	263.7 (72,547)	448.6 (13,890)
120	284.1 (67,465)	446.9 (14,204)	263.7 (66,902)	448.6 (12,433)
150	284.7 (63,028)	436.2 (12,679)	264.3 (64,390)	443.9 (10,505)
180	284.7 (55,967)	435.6 (11,750)	264.9 (63,456)	443.9 (7,615)
210	285.3 (50,120)	435.6 (10,450)	267.3 (63,920)	439.2 (5,105)
240	286.5 (44,460)	433.2 (8,531)	268.5 (63,069)	439.2 (3,853)
270	288.9 (42,275)	432.0 (6,320)	269.7 (63,946)	436.8 (3,759)
300	293.1 (42,025)	429.7 (3,908)	270.3 (62,925)	433.8 (3,713)
330	302.7 (41,845)	429.7 (3,431)	270.3 (62,924)	427.9 (2,697)
360	307.5 (41,588)	429.7 (2,931)	270.3 (62,960)	427.9 (2,579)
390	307.5 (41,075)	429.7 (2,654)	270.9 (62,954)	427.9 (1,434)
420	308.1 (41,083)	429.7 (2,421)	270.9 (62,949)	427.9 (1,322)

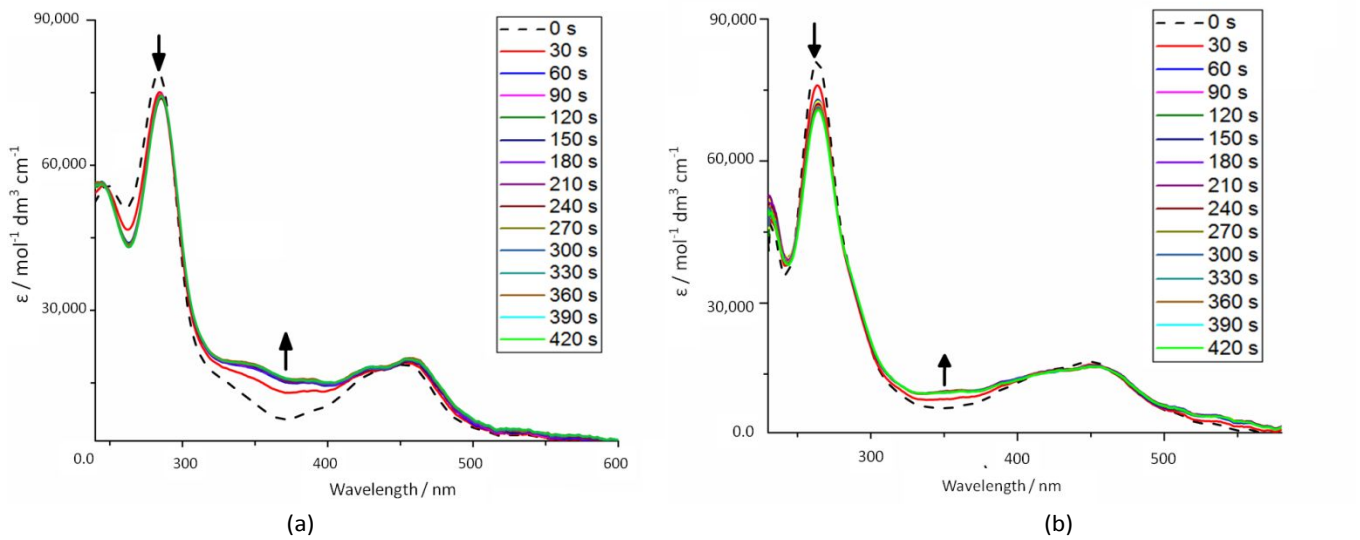

Fig. 9 UV-Vis spectroelectrochemical experiments showing changes with time upon reduction of (a) $[Ru(bpy)_2(phen\text{-}p\text{-}BrBT)]^{2+}$ and (b) $[Ru(phen)_2(phen\text{-}p\text{-}BrBT)]^{2+}$ at −1500 mV vs. Ag/AgCl. The initial spectrum is shown as a dashed black line. Arrows indicate the changes upon one-electron reduction.

Table 9. UV-Vis spectroelectrochemical data as a function of time upon reduction of (a) $[Ru(bpy)_2(phen\text{-}p\text{-}BrBT)]^{2+}$ and (b) $[Ru(phen)_2(phen\text{-}p\text{-}BrBT)]^{2+}$ at −1500 mV *vs.* Ag/AgCl.

	$[Ru(bpy)_2(phen\text{-}p\text{-}BrBT)]^{2+}$		$[Ru(phen)_2(phen\text{-}p\text{-}BrBT)]^{2+}$	
Time / s	Absorption λ_{max} / nm (ε / Lmol^{-1}cm^{-1})		Absorption λ_{max} / nm (ε / Lmol^{-1}cm^{-1})	
0	283.5 (78,537)	363.1 (4,975)	263.7 (80,812)	349.3 (5,883)
30	284.1 (75,212)	363.1 (10,770)	263.7 (76,133)	349.3 (8,288)
60	285.3 (74,923)	363.1 (13,146)	263.7 (72,729)	349.3 (10,499)
90	285.3 (74,920)	363.1 (13,045)	263.7 (72,494)	349.3 (10,500)
120	285.3 (74,897)	363.1 (13,177)	263.7 (72,694)	349.3 (10,500)
150	285.3 (74,815)	363.1 (13,524)	264.3 (72,679)	349.3 (10,501)
180	285.3 (74,811)	363.1 (13,834)	264.3 (72,615)	349.3 (10,501)
210	285.3 (73,773)	363.1 (13,951)	264.3 (72,602)	349.3 (10,503)
240	285.3 (73,764)	363.1 (14,225)	264.3 (72,580)	349.3 (10,503)
270	285.3 (73,746)	363.1 (14,256)	264.3 (72,573)	349.3 (10,507)
300	285.3 (73,680)	363.1 (14,263)	264.3 (72,544)	349.3 (10,509)
330	285.3 (73,668)	363.1 (14,271)	264.3 (72,515)	349.9 (10,511)
360	285.3 (73,593)	363.1 (14,271)	264.3 (72,484)	349.9 (10,511)
390	285.3 (73,547)	363.1 (14,287)	264.3 (72,467)	349.9 (10,511)
420	285.3 (73,528)	363.1 (14,293)	264.3 (72,432)	350.5 (10,513)

3.4.1 Origin of Oxidised- and Reduced-state Electronic Transition: TD-DFT Calculations

The structures of the oxidised and reduced complexes in CH_3CN were calculated by DFT. Vibrational frequency analyses were performed to ensure that the optimised geometries represented local minima and that there were no imaginary frequencies. Calculations were also performed on $[Ru(bpy)_3]^{2+}$ to provide a comparison. The simulated spectra upon oxidation of the $[Ru(bpy)_3]^{2+}$ complex (Fig. 10a) agree reasonably well with the experimental results (Fig. 7a). The intensity of absorption bands in the visible region decreases upon oxidation owing to removal of an electron from the metal centre and a reduction of the MLCT character. Fig. 11 shows the calculated spectroelectrochemical responses upon oxidation of the title complexes. Both complexes exhibit similar variations in their calculated spectra that are comparable to the experimentally observed changes. The intensities of the MLCT bands at 418 and 414 nm are reduced upon oxidation and are blue-shifted to 294 nm and 320 nm for $[Ru(bpy)_2(phen\text{-}p\text{-}BrBT)](PF_6)_2$ and $[Ru(phen)_2(phen\text{-}p\text{-}BrBT)](PF_6)_2$,

respectively (Fig. 11a and Fig. 11b). To further clarify the basis of the blue-shift, an analysis of the frontier MOs of the complexes and their corresponding ligands was carried out. The calculated energy levels and shapes of the MOs that are relevant to the MLCT transitions in the initial and one-electron oxidised states of $[Ru(bpy)_2(phen\text{-}p\text{-}BrBT)](PF_6)_2$ and $[Ru(phen)_2(phen\text{-}p\text{-}BrBT)](PF_6)_2$ portrayed in Fig. 12a and Fig. 12b, respectively. The decrease in electron density on the metal centres results in a blue-shift of the MLCT owing to stabilisation of the Ru-based HOMO. Thus, the energy of the MLCT transition increases upon oxidation. The 294 and 320 nm peaks of $[Ru(bpy)_2(phen\text{-}p\text{-}BrBT)](PF_6)_2$ and $[Ru(phen)_2(phen\text{-}p\text{-}BrBT)](PF_6)_2$ are assigned as MLCT transitions by identifying the ligand character of their LUMOs.

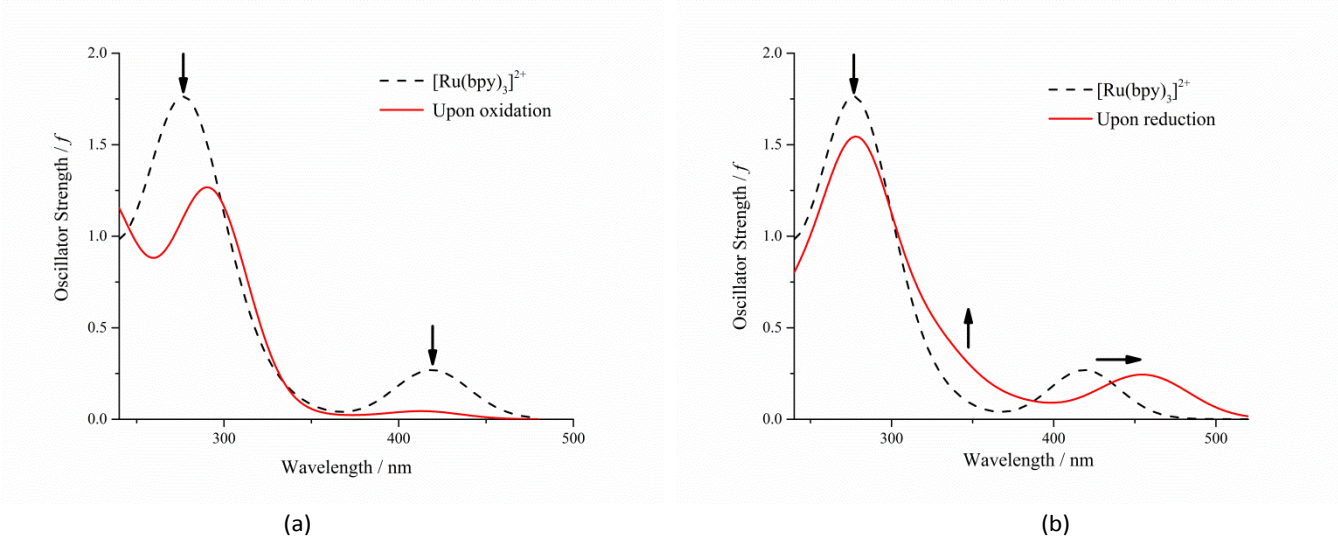

Fig. 10 Calculated spectroelectrochemical responses of $[Ru(bpy)_3)]^{2+}$ upon (a) oxidation and (b) reduction. The initial spectra are shown as a dashed black line. The oxidised and reduced spectra are shown as a full red line, respectively.

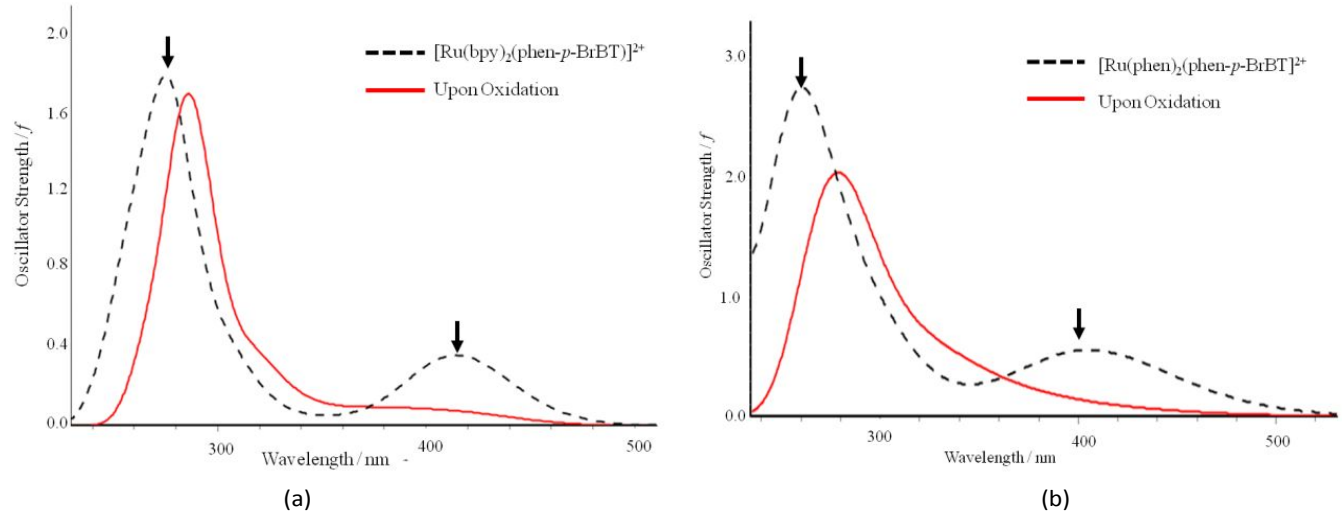

Fig. 11 Calculated spectroelectrochemical responses upon oxidation of $[Ru(bpy)_2(phen\text{-}p\text{-}BrBT)]^{2+}$ (a) and $[Ru(phen)_2(phen\text{-}p\text{-}BrBT)]^{2+}$ (b). The initial spectra are shown as a dashed black line. The oxidised spectra are shown as full red line.

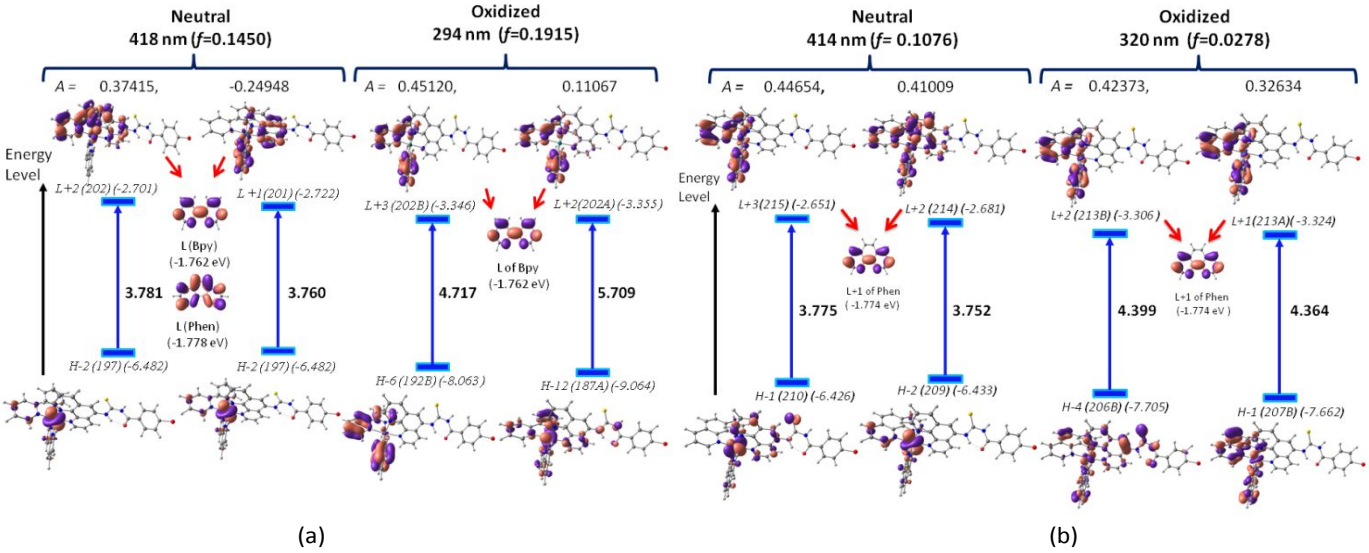

Fig. 12 Calculated energies of the frontier MOs involved in the MLCT transition of initial and one-electron oxidised $[Ru(bpy)_2(phen\text{-}p\text{-}BrBT)]^{2+}$ (a) and $[Ru(phen)_2(phen\text{-}p\text{-}BrBT)]^{2+}$ (b). Orbitals are plotted with a contour value of 0.036 $e^{1/2}$ $Bohr^{-3/2}$.

The spectrum of reduced $[Ru(bpy)_3]^{2+}$ (Fig. 7b) is well reproduced by DFT calculation in Fig. 10b. The absorptions are red-shifted upon reduction, which also distorts the bpy ligand and leads to destabilisation of its HOMO (Fig. 13). However, the calculated spectra of reduced $[Ru(bpy)_2(phen\text{-}p\text{-}BrBT)]^{2+}$ and $[Ru(phen)_2(phen\text{-}p\text{-}BrBT)]^{2+}$ (Fig. 14) show a bathochromic shift in the visible absorption, although there is no obvious change in the observed spectra (Fig. 9). It is expected that addition of an electron to the benzoylthiourea moiety of the title complexes will not shift the experimental MLCT band. However, a red-shifted band is observed in the calculation as a result of adding an electron to the phenanthroline moiety. The discrepancy between the experimental and calculated spectra remains an unanswered question. The character of the electronic transitions is confirmed by TD-DFT calculations of the frontier molecular orbitals of the complexes. $[Ru(bpy)_2(phen\text{-}p\text{-}BrBT)]^{2+}$ shows a red-shift in the MLCT band from 418 to 456 nm upon addition of an electron (Fig. 16). Addition of an electron to the LUMO+1 (phen) of this complex leads to destabilisation of LUMO (phen) and LUMO+1 (phen) relative to LUMO (bpy) and LUMO+1 (bpy). The electrostatic potential of these orbitals is thereby increased, and the MLCT transition takes place from Ru-*d* to LUMO (bpy). The MLCT band of $[Ru(phen)_2(phen\text{-}p\text{-}BrBT)]^{2+}$ is likewise red-shifted from 414 to 446 nm upon reduction (Fig. 17). The LUMO (phen) and LUMO+1 (phen) components of the BT orbital are destabilised relative to LUMO (phen) and LUMO+1 (phen) components of the other phen moieties. Thus, the energies of these orbitals lie above those of the two phen moieties. Consequently, the MLCT transition is attributed to a Ru-*d* to LUMO+1 (phen) transition involving the two unsubstituted phen moieties.

A new broad absorption appears near 350 nm upon reduction of both complexes. This band is tentatively assigned to a second MLCT transition The new band does not correspond to a low energy $n(C{=}S) \rightarrow \pi^*$ transition, because the spectra of the initial complexes also contain a contribution from the $n(C{=}S) \rightarrow \pi^*$ transition (Table 10). The $n(C{=}S) \rightarrow \pi^*$ transition is considered to be a "spectator transition", which does not contribute to the new band that appears upon reduction. The theoretical aspects of the frontier MOs of the complexes were examined to further explore this behaviour. The new absorption band of $[Ru(bpy)_2(phen\text{-}p\text{-}BrBT)]^{2+}$ is assigned to HOMO-3 (Ru-*d*) → LUMO+3 (phen) and HOMO (Ru-*d*) → LUMO+8 (bpy) transitions, as shown in Fig. 16. As discussed earlier, the electrostatic potential of LUMO+1 (phen) is increased upon addition of one electron to LUMO (phen) and LUMO+1 (phen). The energy of the unoccupied phen MO is destabilised, and the new band develops because of the blue-shift of the first MLCT band. It is interesting to note that the red-shift of the 304-nm band in the initial complex also contributes to the appearance of a new band upon reduction, as indicated in Fig. 16. However, for $[Ru(phen)_2(phen\text{-}p\text{-}BrBT)]^{2+}$ the presence of the broad band at 360 nm derives from the blue-shift of the first MLCT band triggered by addition of one electron to LUMO+1 (phen) on the BT moiety (Fig. 17). The band is identified as a combination of the HOMO-3 (Ru-*d*) → LUMO+5 (phen on the BT moiety) and HOMO-4 (Ru-*d*) → LUMO+4 (phen on the BT moiety) transitions. To aid in understanding the blue- or red-shifts produced by reduction, overlaid vertical excitation peaks of initial and one-electron reduced $[Ru(bpy)_2(phen\text{-}p\text{-}BrBT)]^{2+}$ and $[Ru(phen)_2(phen\text{-}p\text{-}BrBT)]^{2+}$ are shown in Fig. 15a and 15b, respectively. To illustrate the details of these interactions, the relevant electronic transitions involving the frontier MOs of $[Ru(bpy)_2(phen\text{-}p\text{-}BrBT)]^{2+}$ and $[Ru(phen)_2(phen\text{-}p\text{-}BrBT)]^{2+}$ and

the corresponding ligands are depicted in Fig, 16 and 17, respectively.

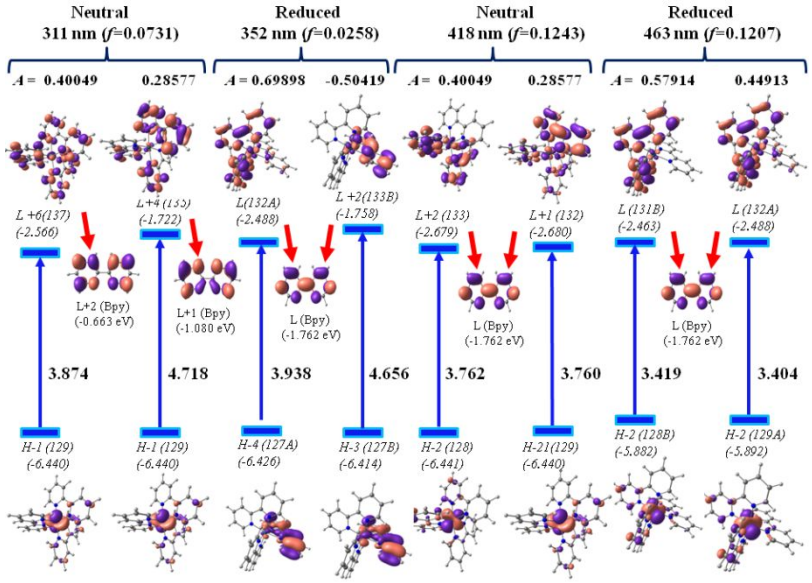

Fig. 13 Calculated energies of the frontier MOs involved in the MLCT transitions at different wavelengths for the initial and one-electron reduced $[Ru(bpy)_3]^{2+}$ complex. Orbitals are displayed with an isovalue of 0.036 $e^{1/2}$ $Bohr^{-3/2}$.

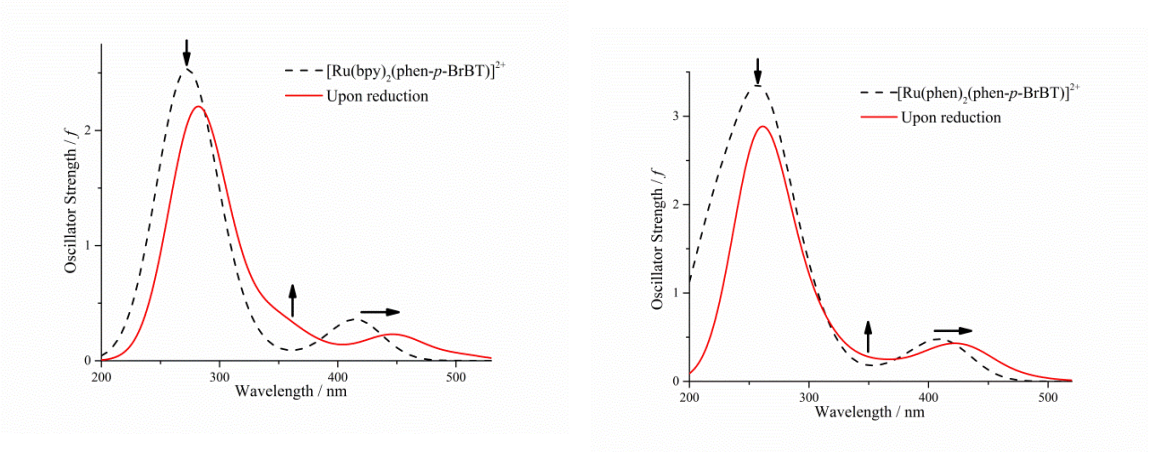

(a) (b)

Fig. 14 Calculated absorption spectra of (a) $[Ru(bpy)_2(phen\text{-}p\text{-}BrBT)]^{2+}$ and (b) $[Ru(phen)_2(phen\text{-}p\text{-}BrBT)]^{2+}$ upon one-electron reduction. The initial spectra are shown as a dashed black line. The spectra of the reduced complexes are shown as a full red line.

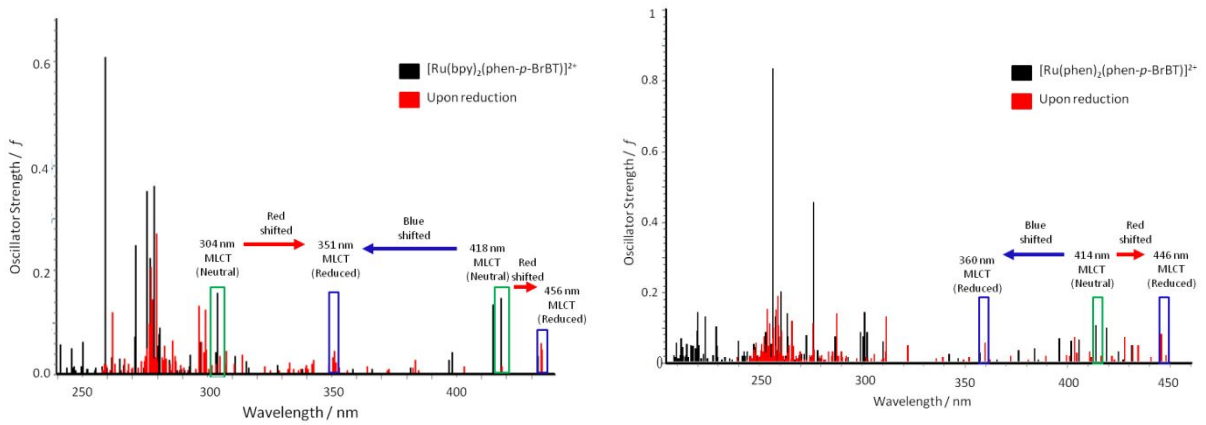

(a) (b)

Fig. 15 A combined representation of the vertical excitation energies and oscillator strengths of initial and one-electron reduced $[Ru(bpy)_2(phen\text{-}p\text{-}BrBT)]^{2+}$ (a) and $[Ru(phen)_2(phen\text{-}p\text{-}BrBT)]^{2+}$ (b).

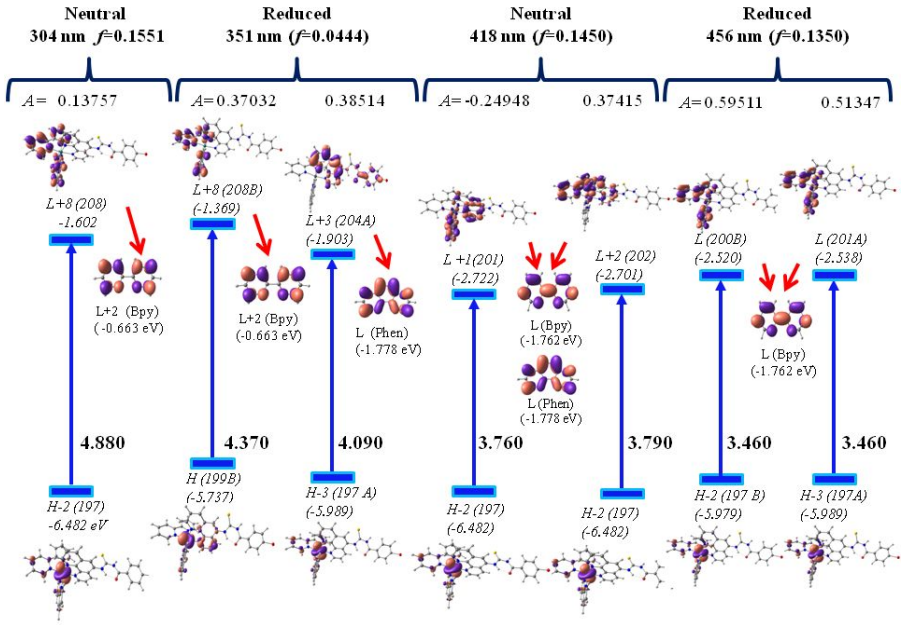

Fig. 16 Calculated energies of the frontier MOs involved in the MLCT transitions at different wavelengths for initial and one-electron reduced $[Ru(bpy)_2(phen\text{-}p\text{-}BrBT)]^{2+}$. Orbitals are displayed with an isovalue of 0.036 $e^{1/2}$ $Bohr^{-3/2}$.

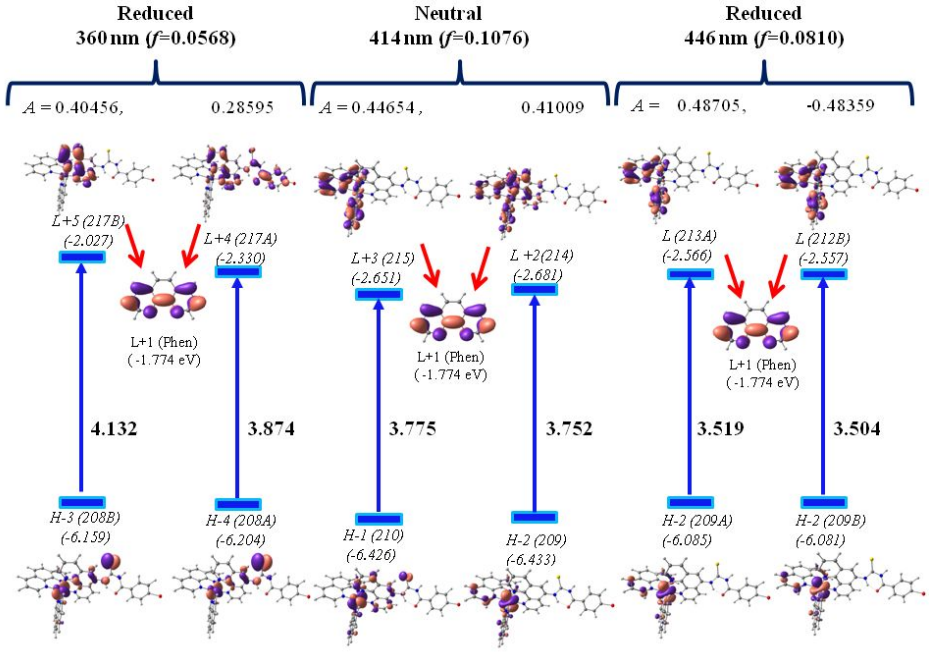

Fig. 17 Calculated frontier MOs of $[Ru(phen)_2(phen\text{-}p\text{-}BrBT)]^{2+}$ at different wavelengths. The orbitals are displayed with an isovalue of 0.036 $e^{1/2}$ $Bohr^{-3/2}$.

Table 10. Orbital contributions (>5%) to the broad transition observed at 351-360 nm in the near UV region.

State (complex); wavelength, nm (highest oscillator strength, *f*)	Composition (%)	Major Contributing Transition	Main character of unoccupied MO
(i)	62	HOMO-3 [*n*(C=S)] → LUMO+4 [π*]	Benzoylthiourea
Initial $[Ru^{II}(bpy)_2(phen\text{-}p\text{-}BrBT)]^{2+}$;	12	HOMO-3 [*n*(C=S)] → LUMO+3 [π*]	LUMO (phen)
358 (0.0094)	10	HOMO-3 [*n*(C=S)] → LUMO+2 [π*]	LUMO (bpy)
	8	HOMO-3 [*n*(C=S)] → LUMO [π*]	LUMO+1 (phen)
(ii)	30	HOMO-3 (Ru-*d*) → LUMO+3	LUMO (phen)
Reduced $[Ru^{II}(bpy)_2(phen\text{-}p\text{-}BrBT)]^{1+}$;	27	HOMO-1 (Ru-*d*) → LUMO+ 8	LUMO+2 (bpy)
351 (0.0444)	19	HOMO-1 (Ru-*d*) → LUMO+3	LUMO (phen)
	14	HOMO-4 (C=S) → LUMO+2	Benzoylthiourea
	13	HOMO-5 (C=S) → LUMO+2	Benzoylthiourea
	10	HOMO-1 (Ru-*d*) → LUMO+6	LUMO+1 (bpy)
	8	HOMO-3 (Ru-*d*) → LUMO+4	LUMO+1 (bpy)
	8	HOMO-3 (Ru-*d*) → LUMO+2	Benzoylthiourea
	7	HOMO (Ru-*d*) → LUMO+7	LUMO+2 (bpy)
	6	HOMO-1 (Ru-*d*) → LUMO+4	LUMO+3 (phen)
	5	HOMO-2 (Ru-d) → LUMO+5	LUMO+1 (bpy)
(iii)	55	HOMO-4 (C=S) → LUMO	LUMO+1 (phen)
Initial $[Ru^{II}(phen)_2(phen\text{-}p\text{-}BrBT)]^{2+}$;	18	HOMO-4 (C=S) → LUMO+1	LUMO (phen)
358 (0.0272)	15	HOMO-3 (C=S) → LUMO+6	Benzoylthiourea
	5	HOMO-3 (C=S) → LUMO+1	LUMO (phen)
(iv)	33	HOMO-3 (Ru-*d* & C=S) → LUMO+5	LUMO+1 (phen)
Reduced $[Ru^{II}(phen)_2(phen\text{-}p\text{-}BrBT)]^{1+}$; 360 (0.0568)	16	HOMO-4 (C=S) → LUMO+4	LUMO+1 (phen)
	15	HOMO-1 (Ru-*d*) → LUMO+5	LUMO (phen)
	15	HOMO-1 (Ru-*d*) → LUMO+5	LUMO (phen)
	11	HOMO-5 (C=S) → LUMO+4	LUMO+1 (phen)
	10	HOMO (Ru-d & C=S) → LUMO+6	LUMO (phen)
	9	HOMO-4 (C=S) → LUMO+4	Benzoylthiourea
	9	HOMO-5 (C=S) → LUMO	LUMO+1 (phen)
	8	HOMO-4 (Ru-*d* & C=S) → LUMO+3	LUMO (phen)
	5	HOMO-1 (Ru-*d*) → LUMO+4	LUMO+1 (phen)
	5	HOMO-1 (Ru-*d*) → LUMO+4	LUMO+1 (phen)
	5	HOMO-3 (Ru-*d* & C=S) → LUMO+4	Benzoylthiourea

4.0 Conclusion

We have presented a combined experimental and theoretical investigation of the changes in the absorption spectra of the $[Ru(bpy)_2(phen\text{-}p\text{-}BrBT)]^{2+}$ and $[Ru(phen)_2(phen\text{-}p\text{-}BrBT)]^{2+}$ complexes upon oxidation and reduction. Analysis of the electronic nature of the constituent ligands identifies the origin of these changes. The results of the study demonstrate the importance of complementing experimental data with theoretical calculations to gain an understanding of the changes in absorption spectra upon addition or removal of an electron. The more highly conjugated system of π-electron delocalisation in 1,10-phenanthroline creates a greater number of excited states, which broadens the absorption band and shifts it toward the visible region. Despite similar electrochemical responses, subtle changes as a function of bpy or phen ligand are observed by UV-Vis spectroelectrochemistry. The decrease in intensity of the visible wavelength band upon removal of an electron supports its assignment as a MLCT transition. The *d*-electron based HOMO is therefore stabilised and displays a hypsochromic shift upon oxidation. The new broad UV band that develops upon reduction is associated with a second MLCT transition and not an *n*(C═S) → π* transition. The new band in $[Ru(bpy)_2(phen\text{-}p\text{-}BrBT)]^{2+}$ originates from a blue-shift of the first MLCT band in the visible region and a red-shift of the band in UV region. However, the new band is assigned only to a blue-shift of the visible-wavelength MLCT band for $[Ru(phen)_2(phen\text{-}p\text{-}BrBT)]^{2+}$. The assignments of electronic transitions in the absorption spectra are supported by analyses of the frontier MOs and electronic distributions in the complexes as functions of ligand structure. It is rewarding that the quantum chemical calculations have successfully clarified the origins of the experimentally observed spectral changes.

Conflicts of Interest

There are no conflicts to declare.

Acknowledgement

S.S.T. would like to acknowledge financial support by Quantum Engineering Design Course (QEDC) Short-Term Research Program by Japan Student Services Organization (JASSO). This work has been partly supported by Grant-in-Aid for Scientific

Research on Innovative Areas "3D Active-Site Science" (No. 26105010 and 26015011) from MEXT, the Advanced Catalytic Transformation Program for Carbon unitization (ACT-C) (Grant No. JPMJCR12YU) of the Japan Science and Technology Agency (JST), Japan, and Ministry of Science Technology and Innovation (06-01-02-SF1001) and Ministry of Higher Education (ERGS/1/2013/TK07/UKM/02/2), Malaysia.

References

1 D. Saha, S, Das, S. Mardanya, S. Baitalik, Structural characterization and spectroelectrochemical, anion sensing and solvent dependence photophysical studies of a bimetallic Ru(II) complex derived from 1,3-di(1H-imidazo[4,5-f][1,10]phenanthroline-2-yl)benzene. *Dalton Trans.* 2012, **41 (29)**, 8886–8898.

2 N. A. F. Al-Rawashdeh, S. Chatterjee, J. a. Krause, W. B. Connick, Ruthenium bis-diimine complexes with a chelating thioether ligand: Delineating 1,10-phenanthrolinyl and 2,2′-bipyridyl ligand substituent effects. *Inorg. Chem.* 2014, **53 (1)**, 294–307.

3 J. G. Małecki, A. Maroní, J. Kusz, Phosphorescence of a ruthenium(II) hydride-carbonyl complex with 3-Hydroxy-2-quinoxalinecarboxylic acid as a co-Ligand. *Mendeleev Commun.* 2015, **25 (2)**, 103–105.

4 L. Tong, R. P. Thummel, Mononuclear Ruthenium Polypyridine Complexes That Catalyze Water Oxidation. *Chem. Sci.* 2016, **7**, 6591-6603.

5 K. Ruffray, M. Autillo, X. Le Goff, J. Maynadié, D. Meyer, Influence of the solvent, structure and substituents of ruthenium(II) polypyridyl complexes on their electrochemical and photo-physical properties. *Inorg. Chim. Acta,* 2016, **440**, 26–37.

6 H. Deng, H. Xu, Y. Yang, H. Li, H. Zou, L. H. Qu, L. N. Ji, Synthesis, characterization, DNA-binding and cleavage studies of $[Ru(bpy)_2(actatp)]^{2+}$ and $[Ru(phen)_2(actatp)]^{2+}$ (actatp=acenaphthereno[1,2-B]-1,4,8,9-tetraazariphenylence). *J. Inorg. Biochem.,* 2003, **97 (2)**, 207–214.

7 L. Mishra, A. K. Yadaw, Synthesis, spectroscopic, electrochemical and luminescence studies of ruthenium (II) polypyridyls containing multifunctionalized 1,2,4-triazole as co-Ligand. *J. Chem. Sci.* 2000, **112 (4)**, 449–458.

8 Y. Tao, Z. J. Lin, X. M. Chen, X. L.; Huang, M. Oyama, X. Chen, X. R. Wang, Functionalized multiwall carbon nanotubes combined with bis(2,2′-bipyridine)-5-amino-1,10-phenanthroline ruthenium(II) as an electrochemiluminescence sensor. *Sens. Actuators, B.* 2008, **129 (2)**, 758–763.

9 W. R. Heineman, Spectroelectrochemistry: The combination of optical and electrochemical techniques. *J. Chem. Educ.,* 1983, **60 (4)**, 305.

10 E. J. Viere, A. E. Kuhn, M. H. Roeder, N. A. Piro, W. S. Kassel, T. J. Dudley, J. J. Paul, J. J. Spectroelectrochemical studies of a ruthenium complex containing the pH sensitive 4,4′-dihydroxy-2,2′-bipyridine ligand. *Dalt. Trans.,* 2018, **47 (12)**, 4149–4161.

11 S. S. Tan, S. Yanagisawa, K. Inagaki, Y. Morikawa, M. B. Kassim, M. B. Augmented pH-sensitivity absorbance of a ruthenium(II) bis(bipyridine) complex with elongation of the conjugated ligands: An experimental and theoretical Investigation. *Phys. Chem. Chem. Phys.,* 2017, **19**, 25734–25745.

12 M. J. Frisch, G. W. Trucks, H. B. Schlegel, G. E. Scuseria, M. A. Robb, J. R. Cheeseman, G. Scalmani, V. Barone, B. Mennucci, G. A. Petersson, H. Nakatsuji, M. Caricato, X. Li, H. P. Hratchian, A. F. Izmaylov, J. Bloino, G. Zheng, J. L. Sonnenberg, M. Hada, M. Ehar, 2009. Gaussian 09 Program Citation.

13 A. D. Becke, Density-Functional Thermochemistry. III. The Role of Exact Exchange. *J. Chem. Phys.* 1993, **98 (7)**, 5648.

14 C Lee, W. Yang, R. G. Parr, Development of the Colle-Salvetti correlation-energy formula into a functional of the electron density. *Phys. Rev. B.* 1988, **37 (2)**, 785–789.

15 C. Jamorski, M. E. Casida, D. R. Salahub, Dynamic polarizabilities and excitation spectra from a molecular implementation of time-dependent density-functional response theory: N_2 as a case study. *J. Chem. Phys.,* 1996, **104 (13)**, 5134.

16 M. E. Casida, C. Jamorski, K. C. Casida, D, R. Salahub, Molecular excitation energies to high-lying bound states from time-dependent density-functional response theory: Characterization and correction of the time-dependent local density approximation Ionization threshold, *J. Chem. Phys.* 1998, **108 (11)**, 4439.

17 M. Cossi, G. Scalmani, N. Rega, V. Barone, New developments in the polarizable continuum model for quantum mechanical and classical calculations on molecules in solution. *J. Chem. Phys.,* 2002, **117 (1)**, 43–54.

18 L. Skripnikov, Chemissian, A computer program to analyze and visualize quantum-chemical calculations; For the current version, S. Chemmisian.

19 B. P. Sullivan, D. J. Salmon, T. J. Meyer, Mixed phosphine 2,2′-bipyridine complexes of ruthenium. *Inorg. Chem.* 1978, **17 (12)**, 3334–3341.

20 R. Shardin, S. S. Tan, M. B. Kassim, Synthesis and structural characterization of *n*-bromobenzoyl-*n*'-(1,10-phenanthrolin-t-yl)thiourea derivatives. *Mal. J. Analy. Sci.*, 2017, **21 (1)**, 60–71.

21 A. G. Orpen, L. Brammer, F. H. Allen, O. Kennard, D. G. Watson, R. Taylor, Tables of bond lengths determined by *X-Ray* and neutron diffraction. *J. Chem. Soc. Dalt. Trans.,* 1987, S1–S83.

22 S. S. Tan, A. A. Al-abbasi, M. I. B. Tahir, M. B. Kassim, Synthesis, structure and spectroscopic properties of cobalt(III) complexes with 1-benzoyl-(3,3-disubstituted)thiourea. *Polyhedron,* 2014, **68**, 287-294.

23 K. L. McCall, J. R. Jennings, H. Wang, A. Morandeira, L. M. Peter, J. R. Durrant, L. J. Yellowlees, J. D. Woollins, N. Robertson, Novel ruthenium bipyridyl dyes with S-donor ligands and their application in dye-sensitized solar cells. *J. Photochem. Photobiol., A Chem.,* 2009, **202 (2–3)**, 196–204.

24 G. Kurt, F. Sevgi, B. Mercimek, Synthesis, characterization, and antimicrobial activity of new benzoylthiourea ligands. *Chem. Pap.* 2009, **63 (5)**, 548–553.

Experimental and Computational Studies on Ruthenium(II) Bis-diimine Complexes of *N*,*N*'-Chelate Ligand: The Origin of Changes in Absorption Spectra upon Oxidation and Reduction

Siew San Tan,*[a,b,c] Susumu Yanagisawa,[e] Kouji Inagaki,[a] Mohammad B. Kassim [a,b,d] and Yoshitada Morikawa [a]

The first report seeking to determine the origin of the observed spectral changes by investigating the frontier MOs and electronic structures of the ligands.